Journal of Laser Applications

RESEARCH ARTICLE | JANUARY 07 2026

Front heating–back sensing in photothermal measurement of cross-plane thermal conductivity: Experimental and theoretical insights

Mahya Rahbar ; Nathan Van Velson ; Xinwei Wang

J. Laser Appl. 38, 012020 (2026)
https://doi.org/10.2351/7.0002004

Journal of Laser Applications ARTICLE pubs.aip.org/lia/jla

Front heating–back sensing in photothermal measurement of cross-plane thermal conductivity: Experimental and theoretical insights

Cite as: J. Laser Appl. 38, 012020 (2026); doi: 10.2351/7.0002004
Submitted: 27 September 2025 · Accepted: 11 December 2025 ·
Published Online: 7 January 2026

View Online Export Citation CrossMark

Mahya Rahbar,[1] Nathan Van Velson,[2] and Xinwei Wang[1,a)]

AFFILIATIONS

[1]Department of Mechanical Engineering, Iowa State University, Ames, Iowa 50011
[2]Research and Development Department, Advanced Cooling Technologies, Inc., Lancaster, Pennsylvania 17601-5688

[a)]**Author to whom correspondence should be addressed:** xwang3@iastate.edu

ABSTRACT

This work presents a modified photothermal (PT) technique to improve the sensitivity in thermophysical property measurements, particularly for materials with a high thermal conductivity and a greater thickness. The modification uses a front heating–back sensing (FHBS) configuration, where a laser irradiates the sample's front surface, while thermal radiation is detected from the back surface. Compared to the previously developed front heating–front sensing (FHFS) PT technique, the FHBS yields weaker signals due to heat penetration through the sample, requiring a sufficiently powerful laser source. The FHBS method is applied to microthick graphene paper and fused silica (SiO_2) samples, yielding out-of-plane thermal conductivities of 4.91 and 1.75 $W\,m^{-1}\,K^{-1}$, respectively. These results agree well with FHFS PT results and literature values, validating the approach. The slight deviation for the SiO_2 sample is attributed to experimental uncertainty in the FHBS configuration, especially in thickness measurement since heat must penetrate deeper in FHBS, making thickness more critical. The FHBS configuration is also tested on a microthick sapphire sample. Although due to sapphire's high thermal conductivity and the limited laser power in our setup, the measurement does not yield reliable data, and the technique remains theoretically feasible with the use of a stronger laser source. This work highlights the importance of selecting an appropriate PT configuration based on the sample's thermal properties and experimental limitations to ensure high accuracy. Moreover, the FHBS PT technique avoids the extreme surface temperature rise often required in the laser flash method, thereby reducing the risk of sample damage and improving suitability for microscale materials.

Key words: photothermal technique, front heating–back sensing, thermal conductivity, microthick samples, sensitivity analysis

I. INTRODUCTION

Efficient thermal management is a common and important challenge in many industries[1] including electronic packaging,[2] energy storage systems,[3] and heat sinks.[4] Therefore, understanding the thermophysical properties of materials, especially thermal conductivity in the out-of-plane direction of microthick samples, is essential for proper heat dissipation, preventing overheating, and improving thermal modeling.[5,6] Since the thermal conductivity in microscale materials can differ from bulk materials due to factors like defect-phonon scattering,[7] several techniques have been developed to measure these properties accurately.

One of the widely used ones for measuring the in-plane thermal conductivity of one-dimensional (1D) nanostructures is the 3ω technique,[8] in which an AC current with an angular frequency of ω is used for heating. This periodic heating generates a temperature variation causing electrical resistance fluctuations at 2ω frequency, thus resulting in a 3ω variation in voltage. The phase shift and amplitude of this voltage variation is used to obtain thermophysical properties of the sample. However, samples need to have an *I-V* linear relation and be electrically conductive. The 3ω technique can also be used to extract the out-of-plane thermal conductivity by varying the frequency of the applied current, which enhances the measurement sensitivity to heat transfer in the out-of-plane direction.[9] However, the sample surface must be sufficiently smooth; otherwise, it must be coated with a thin metallic layer to achieve the required smoothness, which increases the experimental complexity.

The second technique for measuring the out-of-plane thermal diffusivity of few millimeter-thick materials with medium to high thermal conductivities is the laser flash technique, first introduced by Parker *et al.*[10] In this technique, the front surface of the sample is uniformly irradiated by a high-intensity pulsed laser, and the transient temperature rise on the rear surface is recorded. The time required for the rear surface to reach half of its maximum temperature rise ($t_{1/2}$) is then used to calculate the thermal diffusivity of the sample.[11,12] However, for relatively thicker samples, a large temperature rise at the front surface is often required to produce a detectable temperature increase at the rear surface.

The other technique is the differential thermal resistance[13] technique where micro- to millimeter-scale samples are placed between two layers of carbon tape within a thermal circuit to measure their out-of-plane thermal conductivity. This method works well for polymers and plastics with low thermal conductivity. However, it is less suitable for high thermal conductivity materials due to the significant thermal resistance at the sample–carbon tape interface.

Another group of techniques used for measuring thermophysical properties of microthick samples are ultrafast pump-probe techniques. One of the most widely used is the time-domain thermo-reflectance (TDTR) technique,[14] which is effective for both in-plane and out-of-plane measurements. The TDTR uses a high-frequency pulsed laser to heat the sample, followed by cooling. A probe laser is used to detect the surface reflectance, which depends on temperature and can be used to probe the temperature change over time. This surface temperature change is then analyzed to extract the material's thermophysical properties. Because of its short thermal diffusion length, comparable to the laser spot size, the TDTR is particularly sensitive to the out-of-plane thermal conductivity.

The photoacoustic (PA) technique is another method that relates the acoustic response of a sample to modulated light. In this technique, a modulated laser beam heats the sample surface, causing periodic temperature changes that generate pressure (acoustic) waves in the adjacent gas. A microphone detects these signals, which are processed using a lock-in amplifier for thermal analysis. Rosencwaig and Gersho[15] first developed the RG model to describe the heat transfer in PA measurements, followed by the work of Wang *et al.*[16] The photothermal (PT) technique is based on the same heating principle as the PA technique but detects changes in thermal radiation from the sample surface instead of acoustic waves. Our lab has used this technique in multiple studies.[17–20] In the PT method, the phase shift of the detected thermal radiation from the sample surface is used to determine the sample's thermophysical properties. This phase shift depends on the thermal conductivity in the thickness direction and the interfacial thermal resistance (ITR) between different layers in the sample. The PT method used in our lab is based on a front heating–front sensing (FHFS) configuration, where both heating and detection occur on the same surface. While this approach has produced reliable results for low thermal conductivity and small thickness materials, such as SiO_2 and SiC thin-films,[18] organic-inorganic hybrid films [polymethyl methacrylate (PMMA) with SiO_2 or ZrO_2 at varying ZrO_2 concentrations],[19] and vanadium-doped MgH_2,[20] its sensitivity decreases for materials with a higher thermal conductivity, leading to less reliable results.

In this work, we present a modified configuration for the PT technique: a front heating-back sensing (FHBS) configuration. Both FHFS and FHBS follow the same heating principle but differ in how the thermal signal is detected. In the FHFS configuration, a laser is used to irradiate the front surface of the sample (defined as the surface exposed to the laser), which is coated with a metallic layer such as iridium (Ir), and the resulting thermal radiation is collected from the same side. In contrast, the FHBS configuration utilizes a laser to irradiate the Ir-coated front surface, while the thermal radiation is detected from the opposite (back) side of the sample. This back-sensing geometry provides significantly improved sensitivity to thermal conductivity measurement of coating and microscale samples, as will be discussed later.

II. EXPERIMENTAL METHOD AND SETUP

The noncontact PT technique is employed to investigate thermal transport across a multilayer sample.[17,18] The physical principle of this technique is shown in Fig. 1(b). Samples are coated with a 70 nm thick layer of Ir, which serves as an optical absorber for the laser heating. The Ir layer must be sufficiently thick to fully absorb the incident laser and prevent its transmission into the sample. For laser wavelengths of 810 and 1550 nm, the optical absorption depths of Ir are 10.34 and 19.78 nm, respectively, ensuring that the 70 nm coating is optically opaque. A continuous wave laser (BWF2, 810 or 1550 nm wavelength) modulated by a function generator (SRS DS345) is focused onto the Ir surface, inducing periodic heating. This leads to a periodic temperature variation at the Ir surface, which produces modulated thermal radiation. Since the temperature variation at the Ir surface is influenced by the underlying sample's thermal properties, the detected thermal response can be used to extract those properties.

The emitted thermal radiation is collected using an infrared detector [either a photoconductive (PC) detector, Judson J15D12-M204-S01M-60, or photovoltaic (PV) detector, Infrared Associates 469-MCTPV-13-0.5]. A lock-in amplifier (SRS SR830 DSP) measures the phase shift between the thermal signal and the modulated laser input. An antireflective coated germanium (Ge) window is placed in front of the detector to filter out the reflected laser light, ensuring only thermal radiation reaches the sensor. This Ge window has a transmission less than 0.0003% for the wavelengths used in this work. The laser beam has a Gaussian spatial profile and is incident at an angle, resulting in an illuminated spot much larger than the lateral thermal diffusion length. This configuration suppresses the in-plane heat conduction at sufficiently high modulation frequencies, validating the use of a 1D heat conduction model in the analysis of the thermal response.

Figure 1(a) shows a multilayer sample for 1D heat transfer analysis for the PT technique. The structure consists of layer 0 as the substrate and layer $N+1$ as the ambient air, forming a total of $N+2$ layers. The thickness of each layer i is defined as $L_i = l_i - l_{i-1}$. The thermal conductivity k_i, specific heat $c_{p,i}$, thermal diffusivity α_i, optical absorption coefficient β_i, thermal diffusion length $\mu_i \left[= \sqrt{\alpha_i/(\pi f)}\right]$, thermal diffusion coefficient a_i $[= 1/\mu_i]$, and thermal contact resistance between layer i and $i+1$

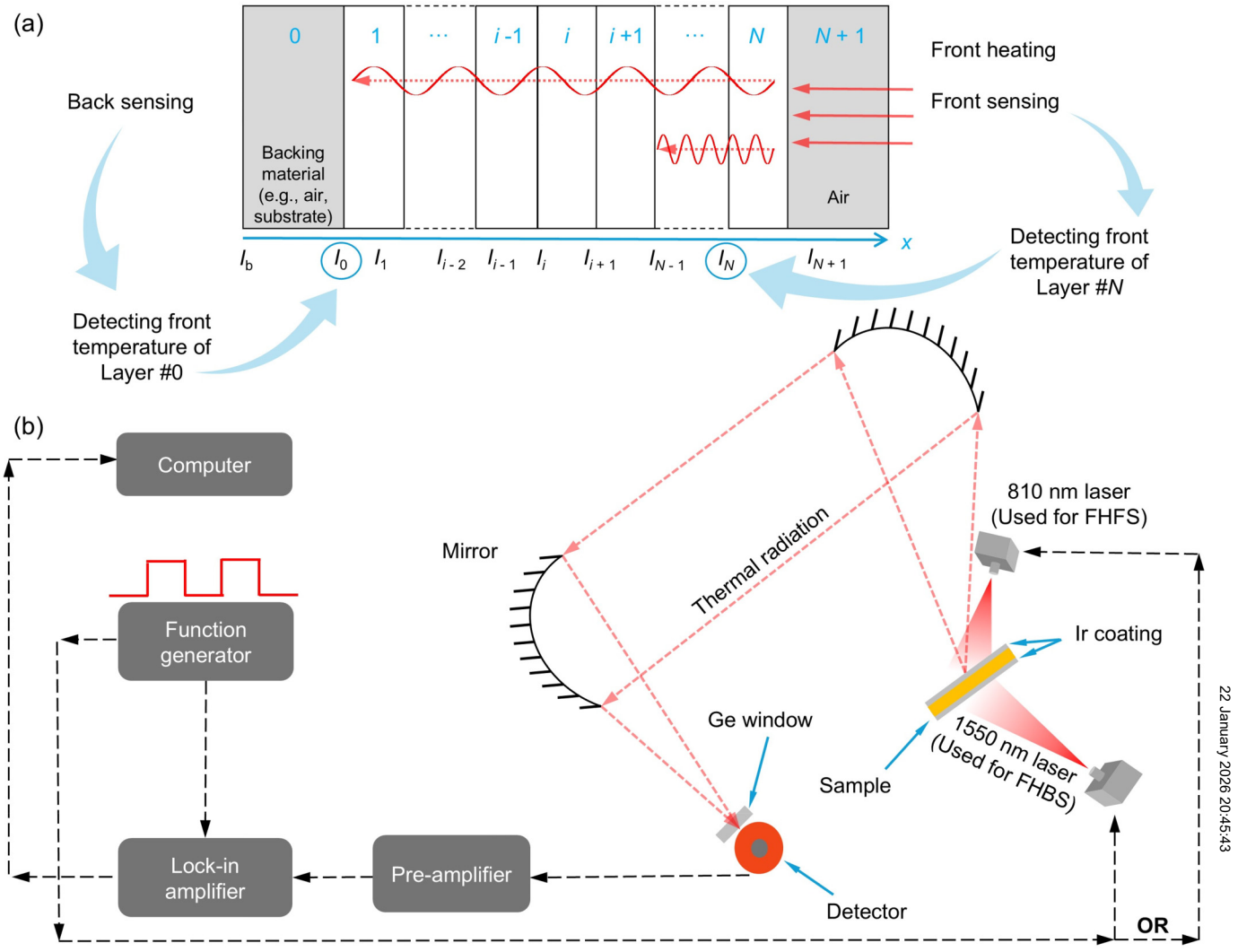

FIG. 1. (a) The schematic of the N-layer sample used in the heat transfer model, and (b) the experimental setup of the PT technique for both FHFS and FHBS configurations.

$R_{i,\,i+1}$ are also used in the heat transfer model. Note that f is the modulation frequency of the incident laser. The governing equation for 1D thermal diffusion in layer i is

$$\frac{\partial^2\theta_i}{\partial x^2}=\frac{1}{\alpha_i}\frac{\partial\theta_i}{\partial t}-\frac{\beta_i I_0}{2k_i}\exp\left(-\sum_{m=i+1}^{N}\beta_m L_m\right)\cdot\exp[\beta_i(x-l_i)]\cdot[1+e^{j\omega t}], \tag{1}$$

where $\theta_i = T_i - T_{\text{amb}}$ is the temperature rise of layer i, T_{amb} is the ambient temperature, and $\omega(=2\pi f)$ is the angular frequency. The solution of Eq. (1) for θ_i includes three components: $\theta_{i,t}$ the transient component that decays as the sample surface reached the thermal steady state condition, the steady DC component $\bar{\theta}_{i,s}$, and the steady AC component $\tilde{\theta}_{i,s}$, which oscillates at the laser modulation frequency. Therefore, only the AC component is relevant for thermal property measurement and is collected by the lock-in amplifier for data processing. The general solution for $\tilde{\theta}_{i,s}$ is

$$\tilde{\theta}_{i,s}=\left[A_i e^{\sigma_i(x-l_i)}+B_i e^{-\sigma_i(x-l_i)}-E_i e^{\beta_i(x-l_i)}\right]e^{j\omega t}, \tag{2}$$

where $E_i = G_i/(\beta_i^2-\sigma_i^2)$ and $G_i=\beta_i I_0\exp\left(-\sum_{m=i+1}^{N}\beta_m L_m\right)/(2k_i)$. Note that for all internal layers $(i<N)$, $G_N=\beta_N I_0/2k_N$ and $G_{N+1}=0$. σ_i is defined as $(1+j)a_i$ and $j=\sqrt{-1}$.

The coefficients A_i and B_i in the temperature solution contain critical information about the thermal and optical properties of the sample. These coefficients are determined through an interfacial transmission matrix of heating (U_i) and absorption matrix of light from layer $i+1$ to i (V_i). Assuming that both ambient air layer (layer $N+1$) and backing material layer (layer 0) are thermally thick (which holds true in our experiment), both A_{N+1} and B_0 are zero. The remaining A_i and B_i coefficients can be determined at $x = l_i$ as

$$\begin{bmatrix} A_i \\ B_i \end{bmatrix} = U_i \begin{bmatrix} A_{i+1} \\ B_{i+1} \end{bmatrix} + V_i \begin{bmatrix} E_i \\ E_{i+1} \end{bmatrix}, \tag{3}$$

$$U_i = \frac{1}{2} \begin{bmatrix} u_{11,i} & u_{12,i} \\ u_{21,i} & u_{22,i} \end{bmatrix}, \tag{4}$$

$$V_i = \frac{1}{2} \begin{bmatrix} v_{11,i} & v_{12,i} \\ v_{21,i} & v_{22,i} \end{bmatrix}, \tag{5}$$

where

$$u_{1n,i} = (1 \pm k_{i+1}\sigma_{i+1}/k_i\sigma_i \mp k_{i+1}\sigma_{i+1}R_{i,i+1}) \cdot \exp[\mp\sigma_{i+1}(l_{i+1} - l_i)], \quad n = 1, 2, \tag{6}$$

$$u_{2n,i} = (1 \mp k_{i+1}\sigma_{i+1}/k_i\sigma_i \mp k_{i+1}\sigma_{i+1}R_{i,i+1}) \cdot \exp[\mp\sigma_{i+1}(l_{i+1} - l_i)], \quad n = 1, 2, \tag{7}$$

$$v_{1n,i} = (-1 \mp \beta_i/\sigma_i), \quad n = 1, 2, \tag{8}$$

$$v_{2n,i} = (-1 \mp k_{i+1}\beta_{i+1}/k_i\sigma_i \mp k_{i+1}\beta_{i+1}R_{i,i+1}) \cdot \exp[-\beta_{i+1}(l_{i+1} - l_i)], \quad n = 1, 2. \tag{9}$$

The final expressions for coefficients A_i and B_i are derived as

$$B_{N+1} = -\frac{[0 \quad 1] \sum_{m=0}^{N} \left(\prod_{i=0}^{m-1} U_i \right) V_m \begin{bmatrix} E_m \\ E_{m+1} \end{bmatrix}}{[0 \quad 1] \prod_{i=0}^{m-1} U_i \begin{bmatrix} 0 \\ 1 \end{bmatrix}}, \tag{10}$$

$$\begin{bmatrix} A_i \\ B_i \end{bmatrix} = \left(\prod_{m=i}^{N} U_m \right) \begin{bmatrix} 0 \\ B_{N+1} \end{bmatrix} + \sum_{m=i}^{N} \left(\prod_{k=i}^{m-1} U_k \right) V_m \begin{bmatrix} E_m \\ E_{m+1} \end{bmatrix}. \tag{11}$$

The PT signal is directly related to the surface temperature of the sample as the emitted thermal radiation is proportional to changes in surface temperature when the temperature rise is small. Using Eq. (2) in the 1D heat transfer model and inputting trial values for unknown parameters, such as thermal conductivity and ITR, the theoretical phase shift for each modulation frequency can be computed. This calculated phase shift is then compared with the experimentally measured values. The sum of the squared difference between theoretical and experimental phase shift values is evaluated. The optimal set of material properties corresponds to the minimum of this sum, yielding the best fit to the experimental data. Note that the front surface is defined as the surface irradiated by the laser. In the FHFS PT configuration, the surface temperature (corresponding to phase shift between thermal radiation and laser beam) of layer N and for FHBS PT configuration, the surface temperature of layer 0 is measured and analyzed.

III. RESULTS

A. System calibration

Before conducting measurements, the PT system must be calibrated to account for any instrumental phase shifts arising from the equipment and optical path, which could otherwise distort the true thermal signal. This calibration phase shift (ϕ_{cal}) is primarily caused by the detector, preamplifier, lock-in amplifier, and laser. During calibration, the Ge window is removed to allow the detector to capture reflected laser light without spectral filtering. By subtracting the calibration phase shift from the measured signal, we ensure that the phase shift originates solely from thermal radiation, eliminating contributions from equipment response. Figure 2 shows the calibration data for both lasers (810 and 1550 nm) and both detectors (PV and PC) used in this work. Note that in our experiment, the direct laser beam is irradiated onto the detector. Since phase shift delays depend on the laser, detector, and lock-in amplifier, separate calibrations are performed for each combination used in this work. Under ideal conditions, without any system-induced delays, the phase shift would be 0° across all modulation frequency. However, due to the presence of frequency-dependent instrument response and time delays, deviations from this ideal behavior are observed. As can be seen, for the 810 nm laser and PC

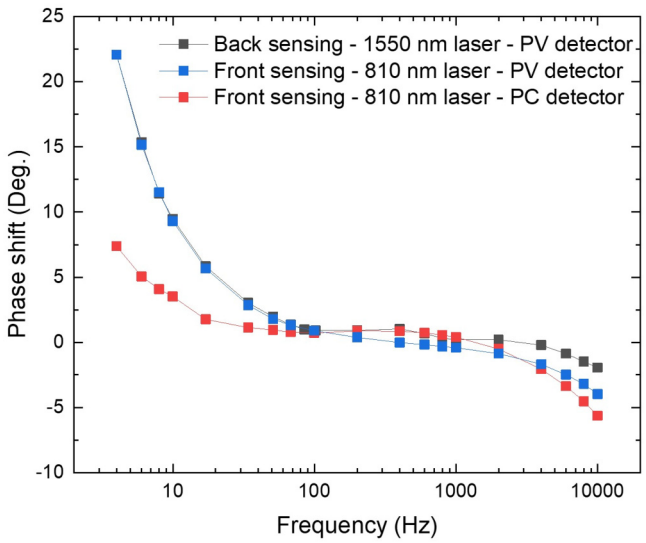

FIG. 2. Calibration phase shifts as a function of modulation frequency for direct laser irradiation onto the PC and PV detectors for both 810 and 1550 nm wavelength lasers.

detector, the phase shift remains near zero degree at low frequencies but increases in magnitude at higher frequencies. This trend is consistent with a fixed system delay, which becomes more noticeable as the frequency increases. For both 810 and 1550 nm lasers paired with the PV detector, the phase shift is relatively large at very low frequencies and then, similar to the 810 nm laser with the PC detector, increases in magnitude at higher frequencies. This suggests that the detector type has a stronger influence on the calibration response than the laser type. The calibrated phase shift difference between the PC detector (paired with 810 nm laser) and the PV detector (paired with both lasers) is clearly distinguishable down to 4 Hz. The time delay (τ) can be estimated as $\tau = \phi/(360f)$. In our experiment, the maximum time delay for the 810 nm laser with PC and PV detectors at frequency of 10 kHz is 1.5 and 1.1 μs, respectively, indicating the signal lags slightly behind the reference signal. The real phase shift of the thermal radiation in the experiment is then calculated as $\phi_{real} = \phi_{exp} - \phi_{cal}$, where ϕ_{exp} is the raw phase shift obtained from the thermal radiation during the experiment. This correction ensures accurate determination of thermophysical properties from the PT measurements.

B. Experimental results and data fitting

In this section, the out-of-plane thermal conductivity of three samples: graphene paper (from Graphene Supermarket), pure SiO_2 (fused silica) (from University Wafer), and sapphire (from Biotin Crystal CO.) are measured using both FHFS and FHBS PT techniques. Each sample is suspended on a copper sheet of high thermal conductivity to ensure efficient heat dissipation. The connection between the sample and copper sheet is secured using silver paste. To enhance the absorption of the incident laser beam, both sides of the SiO_2 and sapphire samples are coated with a 70 nm layer of Ir, but the graphene paper is left uncoated due to its inherently high optical absorption. Figures. 3(a) and 3(b) show the experimental phase shift data and theoretical fittings for graphene paper using FHBS and FHFS PT techniques, respectively, while Figs. 3(c) and 3(d) show the corresponding results for the SiO_2 sample. The blue lines represent theoretical curves corresponding to ±10% of the measured thermal conductivity, showing the fitting uncertainty. To estimate the appropriate modulation frequency range for the experiment, $\delta_\perp = \sqrt{\alpha_\perp/(\pi f)}$ is used, where $\delta_\perp$ is the thermal diffusion length in the out-of-plane direction. For the FHBS PT measurements, the modulation frequency should be sufficiently low such that $\delta_\perp$ is equal to or greater than the sample thickness, ensuring thermal penetration through the sample. In contrast, for the FHFS PT measurements, the frequency should be high enough that the thermal wave decays within the sample, so $\delta_\perp$ is smaller than the sample thickness. An estimated value of $\alpha_\perp$ is used to determine an appropriate frequency range, which is then fine-tuned to optimize the signal-to-noise ratio in the measurements. Note that during our out-of-plane thermal conductivity measurements, the in-plane thermal diffusion length $\delta_\parallel = \sqrt{\alpha_\parallel/(\pi f)}$ is smaller than the laser beam radius, therefore strongly suppressing lateral heat spreading. When a sufficiently large focal spot is used, the diffusion length in the sample remains much smaller than the beam diameter, allowing the PT experiment to be accurately modeled as one-dimensional out-of-plane heat transfer to describe the temperature distribution and its evolution.

The experimental details and measured out-of-plane thermal conductivity values for each sample are summarized in Table I. The sample thickness is measured using a digital micrometer with a resolution of 1 μm, and the ITR reported corresponds to the interface between the sample and Ir coating. For the graphene paper, which is not coated with Ir, the ITR is between the sample and the adjacent air layer. The specific heat value used for the graphene paper is that of graphite. Although graphene paper and graphite have different structures, the difference in their c_p is expected to be minimal.[23] At very low temperatures ($T < 50$ K), the c_p of graphene paper has a linear dependence on temperature due to the dominance of quadratic out-of-plane (ZA) phonon modes. As temperature increases, the c_p follows a T^2 behavior due to the contribution of linear in-plane longitudinal and transverse phonon modes.[24,25] Finally, it reaches a constant value as the temperature approaches the Debye limit. However, the c_p of graphite increases as T^3 at very low temperatures ($T < 10$ K) due to the weak interlayer coupling.[26] Then, at moderate temperature range ($10 < T < 100$ K), its c_p follows the T^2 dependence.[27] Above 100 K, graphene paper has the same c_p as that of graphite. Xie *et al.*[21] measured the ρ of same graphene paper sample to be 1623 ± 55 kg m^{-3} by measuring its mass and volume.

In the FHFS experiments, a PV detector with an 810 nm laser is used for SiO_2 and sapphire, while a PC detector with the same laser is used for graphene paper. For the FHBS experiments, a PV detector paired with a 1550 nm laser is employed. Note that there is no preference for the choice of detector or laser; either combination can be used. The thermal conductivity values obtained from the FHBS PT technique are in good agreement with those measured using the FHFS PT technique developed earlier, demonstrating the reliability of the FHBS method. Furthermore, the results for graphene paper are consistent with the widely accepted range of 5.7–6.8 W m^{-1} K^{-1} for out-of-plane thermal conductivity of graphite.[22] At room temperature (RT), the out-of-plane thermal conductivity of graphene paper is comparable to that of graphite since heat flow in both materials is primarily limited by weak van der Waals interactions.[28] Han *et al.*[29] reported the out-of-plane thermal conductivity of 6.08 ± 0.6 W m^{-1} K^{-1} for the same graphene paper using the pulsed laser-assisted thermal relaxation 2 technique, which closely matches our findings. Moreover, the thermal conductivity of high-purity fused glass (fused silica) is reported as 1.4 W m^{-1} K^{-1}[22] in the mechanical engineer's data handbook, and Combis *et al.*[30] reported a value of 1.38 W m^{-1} K^{-1} at 300 K. Our measured value is slightly higher than these literature values, which could be attributed to experimental uncertainty, particularly since the result obtained using the FHFS PT configuration closely matches the reported data. Another factor contributing to the slight difference between FHFS and FHBS results is the nature of the thermal signal detection in each configuration. In FHFS measurements, the detection occurs near the surface of the sample, making them less sensitive to the sample's overall thickness. In contrast, the FHBS measurements rely on detecting thermal radiation from the back side of the sample, which requires the heat to penetrate deeper. As a result, thickness uncertainty has a greater impact on FHBS measurements.

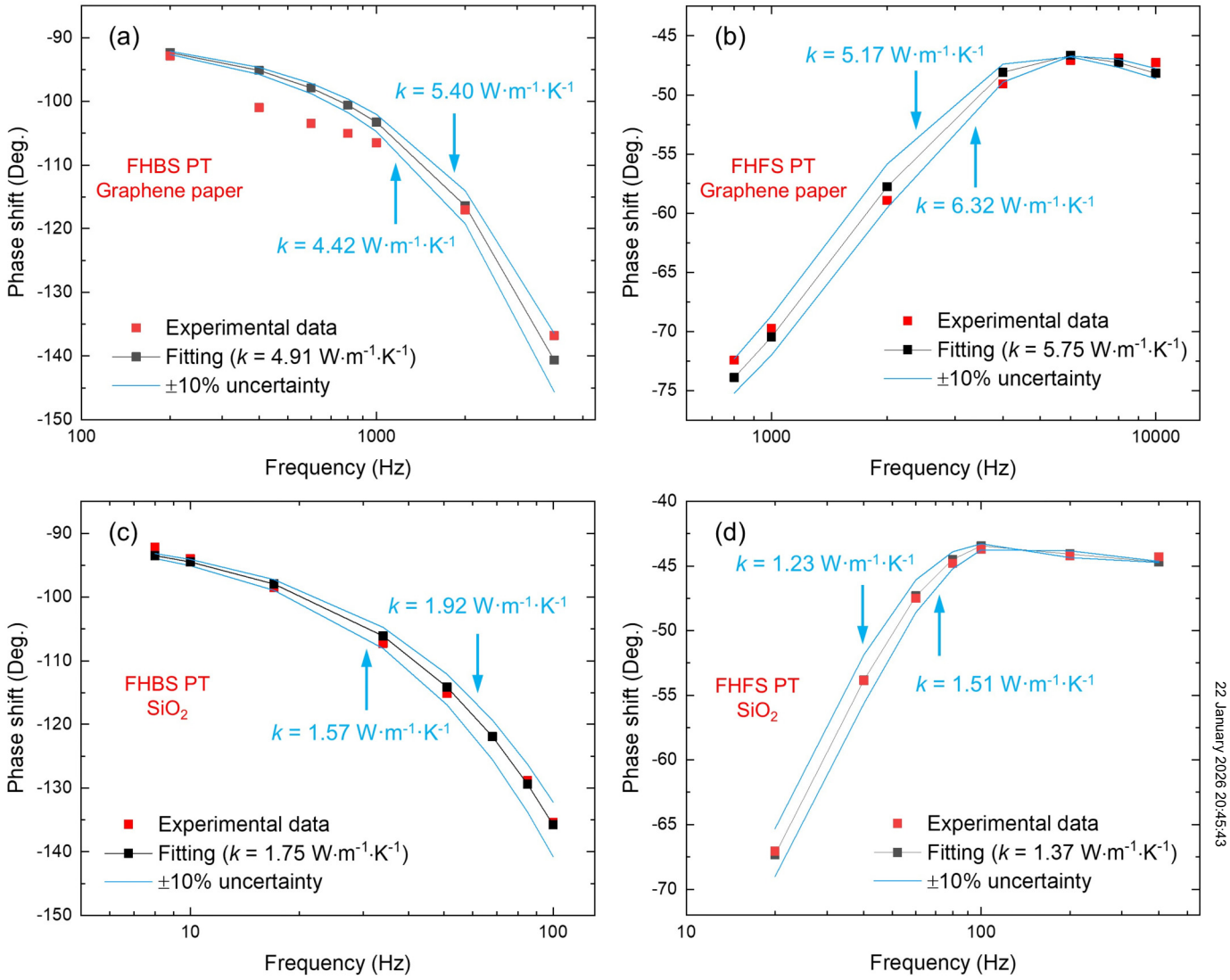

FIG. 3. Data fitting of phase shift for the thermal radiation from the sample surfaces: (a) FHBS PT for graphene paper, (b) FHFS PT for graphene paper, (c) FHBS PT for SiO_2, and (d) FHFS PT for SiO_2. The blue lines represent theoretical curves corresponding to thermal conductivities within ±10% of the measured values for each case, showing the fitting uncertainty. The measured phase shift has an uncertainty of ±0.2°.

TABLE I. Experimental details and thermal conductivity measurement based on phase shift data. Reported thermal conductivities have an uncertainty of ±10%.

Sample	PT type	Thickness (μm)	Density (kg m^{-3})	Specific heat (J kg^{-1} K^{-1})	Thermal conductivity (W m^{-1} K^{-1})	Interfacial thermal resistance (m^2 K W^{-1})
Graphene paper	FHBS	31	1623[21]	709[22]	4.91	N/A
	FHFS				5.75	N/A
SiO_2	FHBS	92	2220[22]	745[22]	1.75	5.4×10^{-9}
	FHFS				1.37	2.2×10^{-7}
Sapphire	FHFS	55	3970[22]	765[22]	18.3	3.8×10^{-7}

Additionally, the frequency used in FHFS is higher than that in FHBS since surface-level heat penetration is sufficient for FHFS, while deeper heat penetration is necessary for FHBS to reach the back surface.

Note that the ITR between the Ir coating and the sample is included as a fitted parameter in our simulation, with the extracted values reported in Table I. The fitted ITR is significantly smaller than the intrinsic thermal resistance of the sample ($R = L/k$: L is the sample thickness and k the thermal conductivity), indicating that its influence on the extracted thermal conductivity is negligible. For graphene samples, the Ir-graphene interface is considered to have an extremely small ITR (in the order of 10^{-9} m^2 K W^{-1}). Therefore, it contributes negligibly to the phase response and has no meaningful impact on thermal conductivity fitting. Moreover, in our fitting model, the Ir coating is also explicitly included with its measured thickness and known thermal properties (thermal conductivity and heat capacity). As a result, the presence of the Ir layer does not influence the extracted cross-plane thermal conductivity of the sample. It simply serves as an additional sample layer that is fully accounted for in the heat transfer solution.

It is worth noting that the Ir coating has a stronger impact on the in-plane thermal conductivity measurements because the coating and the underlying sample act in a parallel thermal transport configuration. In such cases, the apparent in-plane thermal conductivity can be corrected by subtracting the contribution of the metallic layer. This correction procedure has been demonstrated and validated in the work by Alahmad *et al.*[31] Additionally, Ir is commonly used in PT measurements because its high optical absorption and high thermal conductivity help create a uniform, well-defined heating boundary, improving the signal quality without biasing the extracted thermal properties when properly modeled.

We also measured the thermal conductivity of a sapphire sample using FHFS PT technique, as shown in Figure 4. The experimental details and measured thermal conductivity are also reported in Table I. Bai *et al.*[32] reported the thermal conductivity of a 25 μm-thick sapphire sample at RT to be approximately 20 W m^{-1} K^{-1}, which is consistent with our value of 18.3 W m^{-1} K^{-1}. The thermal conductivity of high-purity single-crystal sapphire is reported to be around 50 W m^{-1} K^{-1} at RT.[33] The lower value in our measurement is likely due to phonon scattering caused by defects in the microthick sapphire sample, which reduces thermal conductivity significantly. Bai *et al.*[32] in our lab also determined the structural thermal domain (STD) size of the micrometer-thick sapphire sample using the thermal reffusivity theory. The STD size is a characteristic length that reflects the extent of defect–energy carrier scattering. They obtained an STD size of 85.1 nm for the micrometer-thick sapphire, which is significantly smaller than the values reported in the literature for high-purity sapphire. Specifically, the STD sizes calculated for sapphire samples in the studies by Dobrovinskaya *et al.*[34] and Roy[33] are 2598 and 3445 μm, respectively. This confirms that the micrometer-thick sapphire examined in this work contains a higher level of defects and grain boundaries. The sapphire sample used in Roy's study[33] is high-quality single crystal with much larger dimensions, 3–6 mm in both thickness and length, which explains their lower defect level and the resulting higher thermal conductivity. Therefore, the higher defect level in our sample contributes to the observed reduction in thermal conductivity.

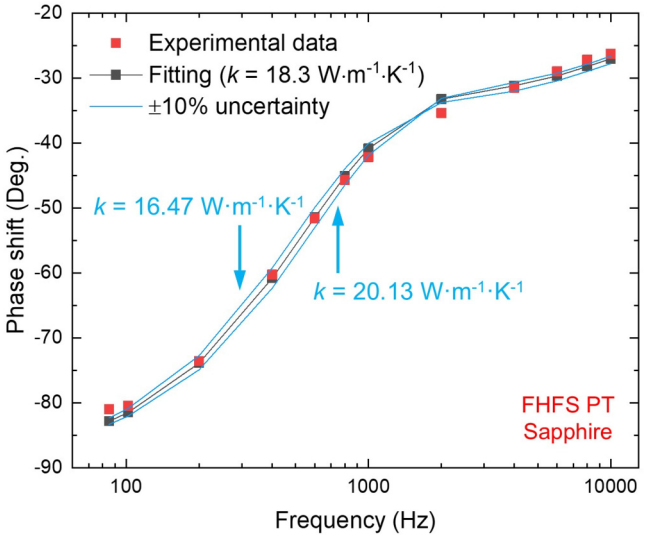

FIG. 4. Data fitting of phase shift from FHFS for the thermal radiation from the sapphire sample surfaces. The measured phase shift has an uncertainty of ±0.2°.

The FHBS PT experiment for the sapphire sample does not yield reliable results. The underlying reason for this observation will be discussed in detail in Sec. IV.

Furthermore, this technique is suitable for microscale materials. However, for nanoscale samples such as few-layered 2D materials, it becomes less practical. Extremely, thin samples require very high modulation frequencies in PT measurements, which shorten the heating period and makes it difficult to achieve an adequate signal-to-noise ratio. In addition, many 2D materials are either optically transparent or have a very long optical absorption depth, thereby requiring deposition of an ultrathin metal coating to absorb the incident light. This process is technically challenging and can alter the 2D material's properties. Therefore, alternative approaches, such as Raman spectroscopy, are more appropriate for characterizing these nanoscale materials.

IV. DISCUSSION

In this section, the sensitivity analysis for both the FHFS and FHBS PT methodologies is presented. Figure 5 shows the theoretical phase shift calculated for a generic sample with a volumetric heat capacity of 3.037×10^6 J m^{-3} K^{-1} across a range of thermal conductivity and thickness. In the simulation, the sample is assumed to be coated with a 70 nm thick Ir layer on both sides and an ITR of 5×10^{-8} m^2 K W^{-1} is considered between the sample and the Ir layer on the front (irradiated) surface. For high thermal conductivity materials, especially at greater sample thicknesses, the FHFS PT methodology shows low sensitivity. This is evident from the phase shift curves in Figs. 5(d)–5(f), where the phase

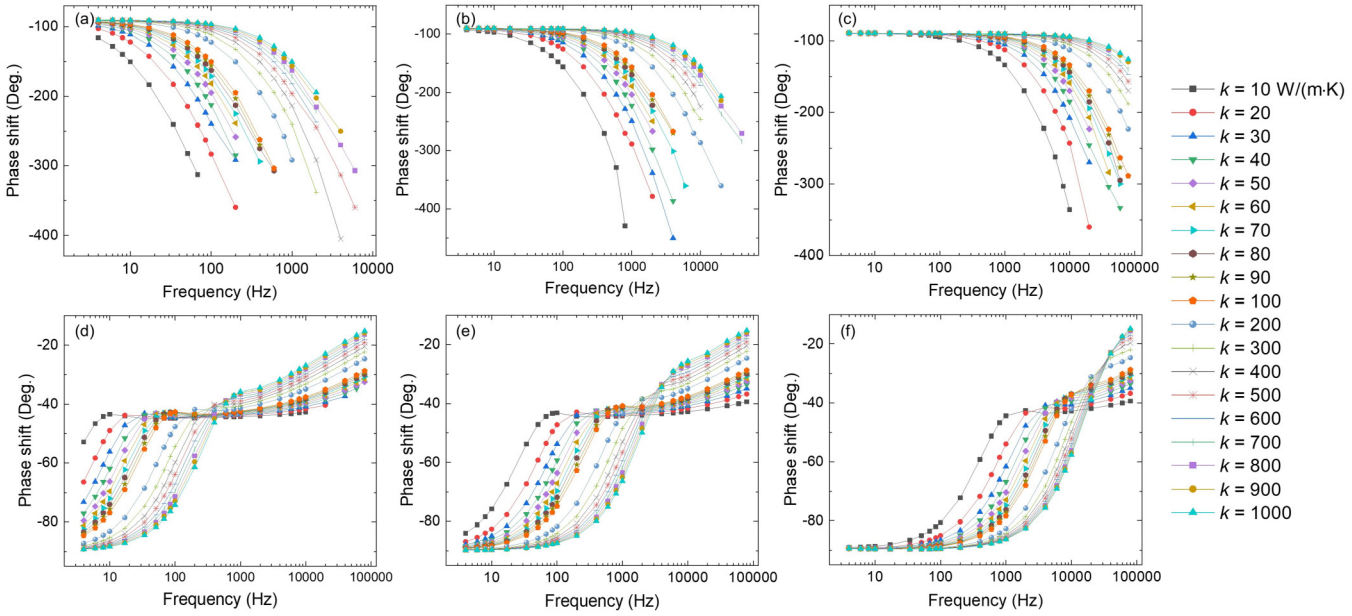

FIG. 5. Sensitivity analysis of FHBS and FHFS PT methodologies based on simulated phase shift vs frequency for a generic sample with a volumetric heat capacity of 3×10^6 J m^{-3} K^{-1} at various thermal conductivity and thicknesses: [(a)–(c)] FHBS configuration for sample thicknesses of 600, 200, and 50 μm, respectively. [(d)–(f)] FHFS configuration for sample thicknesses of 600, 200, and 50 μm, respectively.

shifts become less distinguishable as thermal conductivity increases, particularly above 500 W m^{-1} K^{-1}. The resulting convergence of phase shift curves makes it difficult to accurately extract thermal conductivity, reducing the reliability of the method under these conditions.

On the other hand, the FHBS PT methodology provides greater sensitivity, particularly at higher modulation frequencies and for samples of high thermal conductivity, as shown in Figs. 5(a)–5(c). It highlights the importance of choosing an appropriate configuration based on material properties and experimental constraints. However, this improved sensitivity results in weaker thermal radiation signals, which require a powerful laser to ensure sufficient heating and detectable signal levels. This limitation becomes especially significant for thick or highly conductive samples, where laser penetration and thermal wave generation are more challenging. This trade-off is evident in the case of sapphire: although theoretically suitable for FHBS PT measurement, the method failed in practice due to the insufficient laser power and inability for the heat to transmit through the full sample thickness. In contrast, for lower thermal conductivity materials such as graphene paper or SiO_2 in this work, FHBS shows good sensitivity even at medium frequencies, where radiation signals are stronger and more easily detected. Furthermore, one of the key advantages of the FHBS PT technique over the traditional laser flash method is its ability to avoid extreme surface heating. In the laser flash technique, achieving a detectable temperature rise on the back side of the sample often requires an extremely high front-surface temperature increase, sometimes around 1000 K, which can potentially damage the sample. In contrast, the FHBS PT technique does not require such high temperature rises as the heating occurs over a relatively long time. This makes FHBS PT a safer and more suitable method for microscale samples.

V. CONCLUSION

In this work, a modified version of the PT technique based on FHBS configuration was introduced. In this approach, a laser irradiates the front surface of an Ir-coated sample (either a coating or microscale-thickness material), and the emitted thermal radiation is detected from the back side. This back-sensing configuration offers improved sensitivity for determining thermophysical properties, particularly at higher modulation frequencies and for materials with higher thermal conductivity. However, it tends to produce weaker signals, especially in thicker or highly conductive samples, where sufficient laser penetration and thermal wave generation become more challenging. Therefore, selecting the appropriate configuration based on the sample's properties and experimental limitations is essential. In addition, the FHBS PT technique eliminates the need for extreme surface temperature rises often required in the laser flash method, therefore minimizing the risk of thermal damage and offering a more reliable approach for characterizing microscale samples. We applied the FHBS configuration to microthick graphene paper, SiO_2, and sapphire samples. For graphene paper, the measured out-of-plane thermal conductivity was 4.91 W m^{-1} K^{-1} using FHBS and 5.75 W m^{-1} K^{-1} using FHFS. Similarly, for SiO_2, the values were 1.75 W m^{-1} K^{-1} using FHBS

and 1.37 W m^{-1} K^{-1} using FHFS. These results showed good agreement between the two configurations and with values reported in the literature. A slight discrepancy in the FHBS PT result for the SiO_2 sample is attributed to experimental uncertainty. In contrast, for the sapphire sample, the FHFS configuration yielded a thermal conductivity of 18.3 W m^{-1} K^{-1}, while the FHBS PT measurement failed to provide reliable data. Although theoretically feasible, the high thermal conductivity of sapphire, combined with the limited power of our laser, prevented sufficient heat transmission through the sample thickness, leading to weak or undetectable signals.

ACKNOWLEDGMENTS

We utilized AI-powered tools to check grammar and enhance the academic quality of the text, which was primarily written by the authors. This work was supported by Army Research Office (No. W911NF24P0027).

AUTHOR DECLARATIONS

Conflict of Interest

The authors have no conflicts to disclose.

Author Contributions

Mahya Rahbar: Data curation (lead); Formal analysis (lead); Investigation (lead); Methodology (equal); Writing – original draft (lead). **Nathan Van Velson:** Conceptualization (equal); Formal analysis (equal); Funding acquisition (lead); Investigation (equal); Project administration (lead); Writing – review & editing (equal). **Xinwei Wang:** Conceptualization (equal); Formal analysis (equal); Funding acquisition (equal); Investigation (equal); Methodology (lead); Supervision (lead); Writing – review & editing (equal).

DATA AVAILABILITY

The data that support the findings of this study are available from the corresponding author upon reasonable request.

REFERENCES

[1]Y. Kawagoe, D. Surblys, H. Matsubara, G. Kikugawa, and T. Ohara, "Cross-plane and in-plane heat conductions in layer-by-layer membrane: Molecular dynamics study," Langmuir **36**, 6482–6493 (2020).
[2]V. C. Midhun, M. Maroliya, and S. K. Saha, "Numerical investigation and optimisation of solid–solid phase change material composite-based plate-fin heat sink for thermal management of electronic package," Appl. Therm. Eng. **248**, 123183 (2024).
[3]S. Tian, J. Ma, S. Shao, Q. Tian, Z. Wang, Y. Zhao, B. Tan, Z. Zhang, and Z. Sun, "Estimation of heat transfer performance of latent thermal energy storage devices with different heat transfer interface types: A review," J. Energy Storage **86**, 111315 (2024).
[4]A. D. Abdulsahib, D. Alkhafaji, and I. M. Albayati, "Thermal design and heat transfer analysis of heat sinks and enclosures: A review," Int. J. Heat Technol. **42**, 1149–1163 (2024).
[5]A. R. Dhumal, A. P. Kulkarni, and N. H. Ambhore, "A comprehensive review on thermal management of electronic devices," J. Eng. Appl. Sci. **70**, 140 (2023).
[6]K. Aryana, H. J. Kim, C. C. Popescu, S. Vitale, H. B. Bae, T. Lee, T. Gu, and J. Hu, "Toward accurate thermal modeling of phase change material-based photonic devices," Small **19**, 2304145 (2023).
[7]D. G. Cahill, W. K. Ford, K. E. Goodson, G. D. Mahan, A. Majumdar, H. J. Maris, R. Merlin, and S. R. Phillpot, "Nanoscale thermal transport," J. Appl. Phys. **93**, 793–818 (2003).
[8]J. Hou, X. Wang, P. Vellelacheruvu, J. Guo, C. Liu, and H.-M. Cheng, "Thermal characterization of single-wall carbon nanotube bundles using the self-heating 3ω technique," J. Appl. Phys. **100**, 124314 (2006).
[9]T. Tian and K. D. Cole, "Anisotropic thermal conductivity measurement of carbon-fiber/epoxy composite materials," Int. J. Heat Mass Transfer **55**, 6530–6537 (2012).
[10]W. J. Parker, R. J. Jenkins, C. P. Butler, and G. L. Abbott, "Flash method of determining thermal diffusivity, heat capacity, and thermal conductivity," J. Appl. Phys. **32**, 1679–1684 (1961).
[11]B. Czél, K. A. Woodbury, J. Woolley, and G. Gróf, "Analysis of parameter estimation possibilities of the thermal contact resistance using the laser flash method with two-layer specimens," Int. J. Thermophys. **34**, 1993–2008 (2013).
[12]M. Boutinguiza, F. Lusquiños, J. Pou, R. Soto, F. Quintero, and R. Comesaña, "Thermal properties measurement of slate using laser flash method," Opt. Lasers Eng. **50**, 727–730 (2012).
[13]M. Rahbar, M. Han, S. Xu, H. Zobeiri, and X. Wang, "Development of differential thermal resistance method for thermal conductivity measurement down to microscale," Int. J. Heat Mass Transfer **202**, 123712 (2023).
[14]J. Zhu, X. Wu, D. M. Lattery, W. Zheng, and X. Wang, "The ultrafast laser pump-probe technique for thermal characterization of materials with micro/nanostructures," Nanoscale Microscale Thermophys. Eng. **21**, 177–198 (2017).
[15]A. Rosencwaig and A. Gersho, "Theory of the photoacoustic effect with solids," J. Appl. Phys. **47**, 64–69 (1976).
[16]X. Wang, H. Hu, and X. Xu, "Photo-acoustic measurement of thermal conductivity of thin films and bulk materials," J. Heat Transfer **123**, 138–144 (2001).
[17]X. Wang, Z. Zhong, and J. Xu, "Noncontact thermal characterization of multiwall carbon nanotubes," J. Appl. Phys. **97**, 064302 (2005).
[18]S. Xu and X. Wang, "Across-plane thermal characterization of films based on amplitude-frequency profile in photothermal technique," AIP Adv. **4**, 107122 (2014).
[19]T. Wang, X. Wang, Y. Zhang, L. Liu, L. Xu, Y. Liu, L. Zhang, Z. Luo, and K. Cen, "Effect of zirconium (IV) propoxide concentration on the thermophysical properties of hybrid organic-inorganic films," J. Appl. Phys. **104**, 013528 (2008).
[20]X. Chen, Y. He, Y. Zhao, and X. Wang, "Thermophysical properties of hydrogenated vanadium-doped magnesium porous nanostructures," Nanotechnology **21**, 055707 (2009).
[21]Y. Xie, P. Yuan, T. Wang, N. Hashemi, and X. Wang, "Switch on the high thermal conductivity of graphene paper," Nanoscale **8**, 17581–17597 (2016).
[22]F. P. Incropera, D. P. DeWitt, T. L. Bergman, and A. S. Lavine, *Fundamentals of Heat and Mass Transfer* (Wiley, New York, 1996), Vol. 6.
[23]E. Pop, V. Varshney, and A. K. Roy, "Thermal properties of graphene: Fundamentals and applications," MRS Bull. **37**, 1273–1281 (2012).
[24]J. Hone, "Phonons and thermal properties of carbon nanotubes," in *Carbon Nanotubes: Synthesis, Structure, Properties, and Applications* (Springer, New York, 2001), p. 273.
[25]V. N. Popov, "Low-temperature specific heat of nanotube systems," Phys. Rev. B **66**, 153408 (2002).
[26]R. Nicklow, N. Wakabayashi, and H. Smith, "Lattice dynamics of pyrolytic graphite," Phys. Rev. B **5**, 4951–4962 (1972).
[27]L. X. Benedict, S. G. Louie, and M. L. Cohen, "Heat capacity of carbon nanotubes," Solid State Commun. **100**, 177–180 (1996).
[28]C. Y. Ho, R. W. Powell, and P. E. Liley, "Thermal conductivity of the elements," J. Phys. Chem. Ref. Data **1**, 279–421 (1972).
[29]M. Han, J. Liu, Y. Xie, and X. Wang, "Sub-μm *c*-axis structural domain size of graphene paper uncovered by low-momentum phonon scattering," Carbon **126**, 532–543 (2018).
[30]P. Combis, P. Cormont, L. Gallais, D. Hebert, L. Robin, and J.-L. Rullier, "Evaluation of the fused silica thermal conductivity by comparing infrared thermometry measurements with two-dimensional simulations," Appl. Phys. Lett. **101**, 211908 (2012).

[31]Q. Alahmad, H. Lin, J. Liu, M. Rahbar, T. A. Kingston, and X. Wang, "Characterization of the in-plane thermal conductivity of sub-10 nm Ir films on a flexible substrate," Int. J. Thermophys. **46**, 141 (2025).
[32]J. Bai, A. Karamati, X. Duan, H. Lin, and X. Wang, "Structure thermal domain size in μm-thick single crystalline sapphire wafer uncovered by low-momentum phonon scattering," J. Phys. Chem. C **129**, 5754–5761 (2025).
[33]F. Roy, "Modeling and characterization of coated conductors applied to the design of superconducting fault current limiters," Doctoral thesis (EPFL, Lausanne, 2010), see https://infoscience.epfl.ch/handle/20.500.14299/49471.
[34]E. R. Dobrovinskaya, L. A. Lytvynov, and V. Pishchik, "Properties of sapphire," Sapphire **55**, 55–176 (2009).